Concurrent Optimization of Flight Distance and Robustness of Equipment and Skills in Discus Throwing

Kazuya Seo and Kana Takaoka

Department of Education, Art and Science, Yamagata University, 1-4-12 Kojirakawa, Yamagata, Japan

Keywords: Sports Engineering, Discus, Equipment, Skills in Sports, Robustness, Flight Distance.

Abstract: This paper describes the concurrent optimization of flight distance and 'robustness' of the equipment and skills in a discus. Two objective functions are considered. One is the flight distance, and the other is robustness. Robustness is defined as insensitivity to deviations from the local optimal release conditions. The aim of the optimization is to maximize both the flight distance and the robustness. Fourteen design variables are considered. Eight of the fourteen are concerned with the skill of the thrower. They determine the launch conditions, which are controlled by the thrower when he or she throws. The other six variables are concerned with the design of the equipment. These are the dimensions of the discus, the moment of inertia about the transverse axis and finally mass of the discus. The dependences of size and the angle of attack on the aerodynamic data are estimated by using CFD (computational fluid dynamics) technique. It was found that there is a trade-off between flight distance and robustness. The flight distance is 78.8 meters at the sweet spot solution, where both objective functions have better values simultaneously. The stalling angle for the sweet spot solution is relatively high.

1 INTRODUCTION

Discus throwing is a sport in which the thrower attempts to gain the longest flight distance. In this study, two objective functions are considered (Multi-objective optimization (Deb, 2001)). One is the flight distance, and the other is the robustness. There are fourteen design variables that are considered, including the release conditions (skills), sizes of the discus, the mass and the moment of inertia of the discus (equipment).

Flight distance has usually been treated as the only objective function in the optimization of the discus so far (Hubbart and Cheng, 2007). Generally, it is considered that there are many local longest flight distances (= local optimal solutions) with respect to the design variables. Some of local longest flight distances are sensitive to changes in the design variables. This sensitivity is a difficult problem for throwers. The thrower sometimes makes mistakes when trying to achieve the global optimal release condition. The thrower is not a robot, but a human. Therefore, robustness is also important, especially for the world of competitive sports. Here, robustness can be defined as insensitivity to deviations from the local optimal release conditions.

2 FLIGHT TRAJECTORY

2.1 Inertial Coordinate System

The inertial coordinate system is shown in Figure 1. The origin is defined as being at the center of the throwing circle, while the X_E-axis is in the horizontal forward direction, the Y_E-axis is the horizontal lateral direction and the Z_E-axis is vertically downward.

2.2 Body-fixed Coordinate System

The coordinate system in the discus body-fixed system is denoted by x_b, y_b and z_b (Figure 2-c). The origin is defined as the center of gravity of the discus. It is assumed that the geometric center of the discus coincides with the center of gravity, that its z_b axis is aligned with the transverse axis (axis of symmetry), and that x_b and y_b are aligned with the longitudinal axes in the discus planform. Assuming that the origin of the inertial coordinate system (X_E, Y_E, Z_E) is displaced without any rotation to the center of gravity of the discus, the new reference frame is defined as (X_0, Y_0, Z_0) in Figure 2-a. The sequence of

rotations conventionally used to describe the instantaneous attitude with respect to an inertial coordinate system is shown in Figure 2 (Stevens and Lewis, 2003). Starting with (X_0, Y_0, Z_0) the following sequence is followed; 1) Rotate about the Z_0 axis, nose right (positive yaw Ψ, Figure 2-a), 2) Rotate about the y_1 axis, nose up (positive pitch Θ, Figure 2-b), 3) Rotate about the x_b axis, right wing down (positive roll Φ, Figure 2-c).
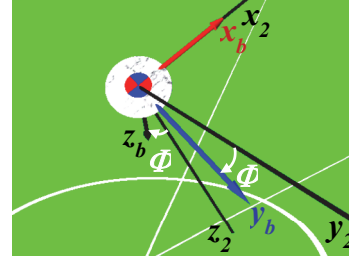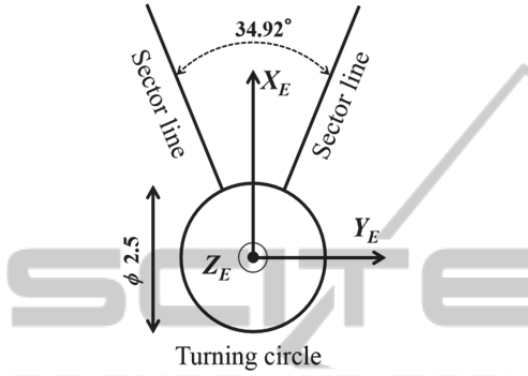

Figure 1: The inertial coordinate system. The origin is defined as being at the center of the turning circle, while the X_E-axis is in the horizontal forward direction, the Y_E-axis is the horizontal lateral direction and the Z_E-axis is vertically downward.
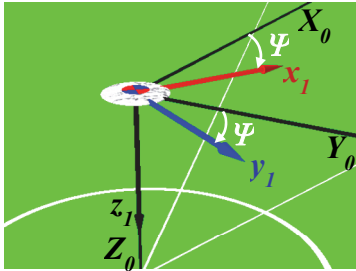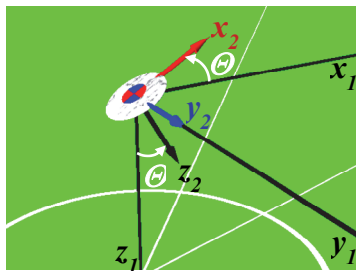

Figure 2-a: Definition of Ψ.

Figure 2-b: Definition of Θ.

Figure 2-c: Definition of Φ.

Figure 2: Definitions of Euler angles that are used to describe the instantaneous attitude with respect to the inertial coordinate system.

2.3 Flight Trajectory Simulation

Since there is a mathematical singularity (Gimbal lock) at $\Theta = 90°$, quaternion parameters (q_0, q_1, q_2, q_3) should be used instead of Euler angles when the flight trajectory is simulated. Therefore, the initial set of Euler angles is first transformed into the initial quaternion parameters by Equations (1) through (4) (Stevens and Lewis, 2003).

$$q_0 = \cos(\Phi/2) \cdot \cos(\Theta/2) \cdot \cos(\Psi/2) + \sin(\Phi/2) \cdot \sin(\Theta/2) \cdot \sin(\Psi/2) \tag{1}$$

$$q_1 = \sin(\Phi/2) \cdot \cos(\Theta/2) \cdot \cos(\Psi/2) - \cos(\Phi/2) \cdot \sin(\Theta/2) \cdot \sin(\Psi/2) \tag{2}$$

$$q_2 = \cos(\Phi/2) \cdot \sin(\Theta/2) \cdot \cos(\Psi/2) + \sin(\Phi/2) \cdot \cos(\Theta/2) \cdot \sin(\Psi/2) \tag{3}$$

$$q_3 = \cos(\Phi/2) \cdot \cos(\Theta/2) \cdot \sin(\Psi/2) - \sin(\Phi/2) \cdot \sin(\Theta/2) \cdot \cos(\Psi/2) \tag{4}$$

The force equations and moment equations of motion in the discus body-fixed system are denoted by Equations (5) through (10).

$$\dot{U} = \frac{1}{m_d}\left[X_a + 2m_d g(q_1 q_3 - q_0 q_2)\right] - QW + RV \tag{5}$$

$$\dot{V} = \frac{1}{m_d}\left[Y_a + 2m_d g(q_2 q_3 + q_0 q_1)\right] - RU + PW \tag{6}$$

$$\dot{W} = \frac{1}{m_d}\left[Z_a + m_d g\left(q_0{}^2 - q_1{}^2 - q_2{}^2 + q_3{}^2\right)\right] - PV + QU \tag{7}$$

$$\dot{P} = \frac{L_a}{I_L} - QR\left(\frac{I_T}{I_L} - 1\right) \tag{8}$$

199

$$\dot{Q} = \frac{M_a}{I_L} - RP\left(1 - \frac{I_T}{I_L}\right) \qquad (9)$$

$$\dot{R} = \frac{N_a}{I_T} \qquad (10)$$

Here, (U, V, W), (P, Q, R), (X_a, Y_a, Z_a) and (L_a, M_a, N_a) are the (x_b, y_b, z_b) components of the velocity vector, the angular velocity vector, the aerodynamic forces and the aerodynamic moments, respectively. The mass of the discus is denoted by m_d, and the gravitational acceleration is denoted by g. The moments of inertia about the transverse axis and the longitudinal axis are denoted by I_T and I_L. Due to the symmetry of the discus, the principal moments of inertia on the x_b and y_b axes are set to $I_{xx}=I_{yy} = I_L$ in Equations (8) through (10), and the cross inertia terms are zero. The aerodynamic forces (X_a, Y_a, Z_a) and moments (L_a, M_a, N_a) are derived from C_D, C_L and C_M on the basis of the cross product (Seo, et al, 2010). Aerodynamic coefficients, C_D, C_L and C_M are estimated by using CFD (computational fluid dynamics) technique, which will be described in the next section. Other aerodynamic coefficients are assumed to be 0.

The derivatives of the quaternion parameters are expressed by the angular velocity vector (P, Q, R) (Stevens and Lewis, 2003).

$$\dot{q}_0 = 0.5\left(- Pq_1 - Qq_2 - Rq_3\right) \qquad (11)$$

$$\dot{q}_1 = 0.5\left(Pq_0 - Qq_3 + Rq_2\right) \qquad (12)$$

$$\dot{q}_2 = 0.5\left(Pq_3 + Qq_0 - Rq_1\right) \qquad (13)$$

$$\dot{q}_3 = 0.5\left(- Pq_2 + Qq_1 + Rq_0\right) \qquad (14)$$

In terms of coordinate transformations we then have

$$\begin{pmatrix} \dot{X}_E \\ \dot{Y}_E \\ \dot{Z}_E \end{pmatrix} = [m_{ij}] \begin{pmatrix} U \\ V \\ W \end{pmatrix} \qquad (15)$$

Here, $[m_{ij}]$ is the Euler-angle transformation matrix (Stevens and Lewis, 2003). The flight trajectory $(X_E(t), Y_E(t), Z_E(t))$ can be obtained by integrating Equations (5) through (15) numerically.

3 ESTIMATING AERODYNAMIC COEFFICIENTS

3.1 CFD

In order to understand the dependence on the size of the discus of the aerodynamic forces, it is necessary to study many discuses of various sizes. In this study, the CFD technique was applied to estimate the aerodynamic forces.

A discus was initially developed using Ansys DesignModeler. It had the same width (w) of 181.5mm, thickness (*THK*) of 37mm, metal rim radius (R_{MR}) of 6.15mm and diameter of the flat center area *(D_{FCA})* of 50mm as the competition discus (Super HM, Nishi Athletics Goods). A cube in which all 12 edges are 4000mm, was constructed around the discus as an enclosure. The frontal area of the cube was defined as a velocity inlet, while the rear of the cube was set as a pressure outlet where the airflow exits. The rest of the boundaries were defined as walls. These were then imported to Ansys Meshing, a pre-processor of CFD code FLUENT. Hybrid meshes of tetrahedrons and hexagons were used. The size function and the inflation controls were also used to mesh the volumes. If the number of cells were more than one million, then the aerodynamic coefficients determined by CFD would agree with those determined by EFD. However, the computing time for CFD is more than three hours for just one case. Here, there are hundreds of cases to be calculated. Since the computing time is also important, the number of cells was set 213,314 by local inflation settings. It takes about 30 minutes to estimate aerodynamic coefficients (Core i7-960, 3.2GHz, 6 cores). In this case, the values of (C_D, C_L, C_M) = (0.23, 0.71, 0.18) at *AoA*=25° and 30ms^{-1} are almost same as those (C_D, C_L, C_M) = (0.23, 0.74, 0.18) determined by the fine mesh (1,171,589 cells). The average skewness in the case of 213,314 cells was 0.25. The growth rate was 1.2.

The aerodynamic forces in the steady flow state were calculated by FLUENT 14.0. Comparisons between EFD and CFD at *AoA*=25° and 30ms^{-1} are shown in Figure 3. The ordinates are the ratio between CFD and EFD. If CFD/EFD is equal to 1, the aerodynamic coefficients derived by CFD coincide with those obtained by EFD. The abscissa shows four combinations of RANS-based turbulence model and wall treatments. It can be seen that C_D and C_L derived by CFD are all smaller than those derived by EFD. The combination of the standard k-epsilon (ske) model and the enhanced wall treatment

(ewt) gives the best agreement with EFD, though C_M derived by CFD is 20% larger than that by EFD. Moreover, the standard k-epsilon model is robust.
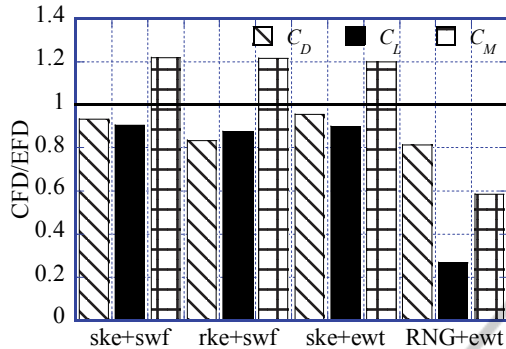

Figure 3: Comparisons of aerodynamic coefficients between CFD and EFD. AoA=25° and U=30 ms^{-1}. ske=standard k-epsilon, rke=realizable k-epsilon, swf=standard wall function, ewt=enhanced wall treatment.

Therefore, the standard k-epsilon model with the enhanced wall treatment was used for the turbulence modelling. The second-order upwind method was selected for all equations, and the convergence criterion for continuity equations was set as 10^{-3}.

3.2 Comparison between EFD (Experimental Fluid Dynamics) Results and CFD Results

Comparisons between the EFD results and the CFD results is shown in Figure 4. The aerodynamic coefficients, C_D, C_L and C_M, as a function of AoA are shown. The definition of the drag coefficient, C_D, is the drag divided by the dynamic pressure and the area of the discus planform. The lift coefficient, C_L, and the pitching moment coefficient, C_M, are defined in the same manner. Since there is little difference between aerodynamic coefficients for wind speeds in the ranges from 15 to 30 ms^{-1} and from 0 to 7 revolutions per second (Seo et al., (2012)), the data at 30 ms^{-1} and 0 revolutions per second are shown with error bars. The open circles denote EFD results from wind tunnel tests during the process of increasing AoA from 0° to 90°, while the open triangles show the process when decreasing AoA from 90° to 0°. The closed diamonds show CFD results. It can be seen that the aerodynamic coefficients obtained by CFD qualitatively agree with those obtained by EFD. In the experiments, there are differences in C_L and C_M in the process of decreasing AoA, compared with the data when the process is increasing. Therefore, hysteresis occurs in C_L and C_M in the experiments. On the other hand,
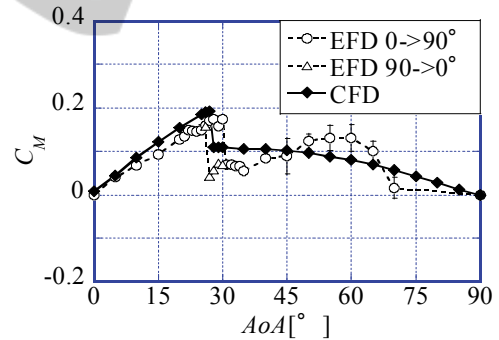
CFD could not detect the hysteresis in C_L and C_M so far, though it could detect the effect of the stall.
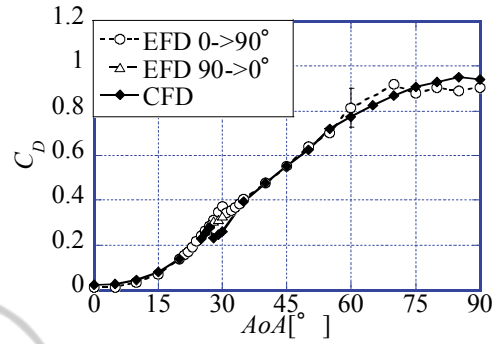
(a). The drag coefficient, C_D.
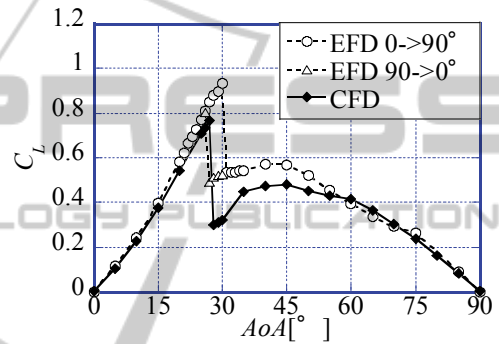
(b). The lift coefficient, C_L.

(c). The pitching moment coefficient, C_M.

Figure 4: AoA dependence of aerodynamic forces.

3.3 Estimating Aerodynamic Coefficients

Aerodynamic forces were calculated by CFD for 247 cases, in which AoA and the size (D_{FCA}, R_{MR}, THK and w) in Figure 5 were changed. The size was varied in the design regulations for the discus, and AoA was varied from 0° to 90°. In order to estimate aerodynamic forces with respect to an arbitrary set of values (D_{FCA}, R_{MR}, THK and w), the concept of 'inverse distance weighting interpolation' was applied. Inverse distance weighted interpolation are

201

based on the assumption that the interpolating surface should be influenced most by the nearby points and less by the more distant points. There are four procedures. At first, each variable in the arbitrary set and in all of the 247 cases were normalized, respectively. The second procedure is to calculate the Euclidean distance between the normalized arbitrary set and each of 247 the normalized cases. The third procedure is to find the shortest Euclidean distance, l_i, and the second shortest Euclidean distance, l_j. The forth procedure is to estimate the aerodynamic forces from the known CFD results on the basis of l_i and l_j. Defining the subscript i as the shortest Euclidean distance and the subscript j as the second shortest Euclidean distance, the drag coefficient, C_D, can be estimated from the 247 known CFD results in Equation (16). The lift coefficient, C_L, and the pitching moment coefficient, C_M, can be estimated in the same manner.

$$C_D\left(D_{FCA}, R_{MR}, THK, w\right)$$
$$= \frac{1}{l_i + l_j}\left[l_j \cdot C_D\left(D_{FCA,i}, R_{MR,i}, THK_i, w_i\right)\right.$$
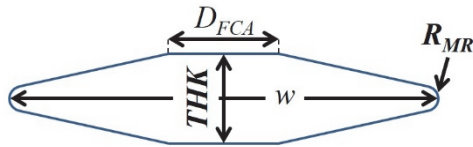$$\left. + l_i \cdot C_D\left(D_{FCA,j}, R_{MR,j}, THK_j, w_j\right)\right] \quad (16)$$

Figure 5: Design variables concerned with the size of the discus.

4 OPTIMIZATION

4.1 Objective Function

The flight distance, which is considered to be the first objective function, is defined as in Equation (17).

$$F1 = -\sqrt{X_E\left(t_f\right)^2 + Y_E\left(t_f\right)^2} \quad (17)$$

$$F2 = \sqrt{\frac{\sum_{i=1}^{n}\left(FD_i - FD_{candidate}\right)^2}{n-1}} \quad (18)$$

The flight time is denoted by t_f. In the optimization process, $F1$ should be minimized because of the negative sign on the right hand side.

On the other hand, robustness is considered as the second objective function. Robustness is defined as the insensitivity to deviations from the local optimal release and equipment conditions at the local longest flight distance. In this study, the standard deviation around the local optimal solution is considered to be the second objective function, which is defined in Equation (18). The concept of robustness is explained by Figure 6, which shows a contour map of the flight distance with respect to two arbitrary design variables. The local longest flight distance, $\times$, is denoted by $FD_{candidate}$ in Equation (18). Here, FD stands for the flight distance. The points denote the flight distances, FD_i, around $FD_{candidate}$. The circle shows the range of design variables corresponding with the human error or the manufacturing error. Therefore, estimating $F2$ requires many trajectory simulations around $FD_{candidate}$. The number of trajectory simulations with respect to sets of initial conditions around $FD_{candidate}$ is denoted by n in Equation (18).

In the optimization process, both objective functions should be minimized. The optimization is carried out with the aid of an adaptive range genetic algorithm (Sasaki et al. (2005)). The population for each generation is 500, and the number of generations is also set to 700.
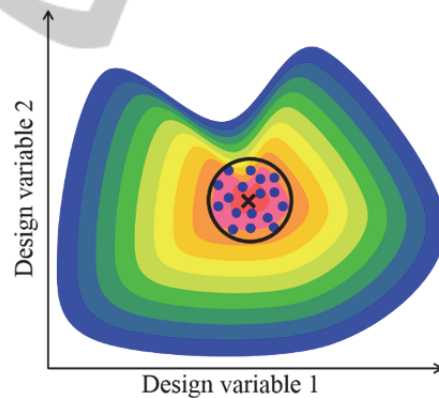

Figure 6: The concept of 'robustness'. Contour map of the flight distance with respect to two arbitrary design variables. The local longest flight distance is denoted by $\times$. The points, $\bullet$, denote the flight distances around $\times$. The circle shows the range of design variables corresponding with the human error or the manufacturing error. The standard deviation of $\bullet$ is defined as robustness.

4.2 Design Variables

The fourteen design variables are shown in Table 1. The 'ranges for GA', which are also shown in Table 1, are defined such that they can cover practical values for the skill level of the thrower (Leigh et al.

(2010)) and the design regulations for the discus. Eight of the variables, from γ to R in Table 1, are concerned with the skill of the thrower at the point of launch. The other six, from I_T to w, are concerned with the equipment, which are controlled by the designer. In this study, concurrent optimization of both the thrower's skill and the equipment is carried out. Since the linear relationship between I_L (Moment of inertia on the longitudinal axis) and I_T is derived from CAD data, I_L can be uniquely determined in accordance with I_T.

Table 1: Design variables.

Design variables	Abb.	Ranges for GA	Ranges for MC
Flight path angle	γ	15～60°	±5°
Azimuth angle	X	-30～30°	±5°
Roll angle	Ψ	-45～45°	±5°
Pitch angle	Θ	-60～60°	±5°
Yaw angle	Φ	-45～45°	±5°
Spin rate about the x_b axis	P	-3～3 rev/s	±0.1 rev/s
Spin rate about the y_b axis	Q	-3～3 rev/s	±0.1 rev/s
Spin rate about the z_b axis	R	0～7rev/s	±0.1 rev/s
Moment of inertia on the transverse axis	I_T	0.0055～0.006 kgm²	±0.0001 kgm²
Mass	m_D	1.005～1.025 kg	±5 g
Diameter of the flat center area	D_{FCA}	50～57 mm	±0.1 mm
Radius of the metal rim	R_{MR}	5.85～6.45 mm	±0.1 mm
Thickness	THK	37～39 mm	±0.1 mm
Width	W	180～182 mm	±0.1 mm

Since a right-handed thrower is assumed, the launch position is considered to be in the right-hand side of the throwing circle. The launch position is assumed to be $(X_E, Y_E, Z_E) = (1.0, 1.0, -1.6)$ in this study. The negative sign of Z_E means the vertically upward direction, and the value of -1.6 is almost the highest launch position achievable for women. The release height is generally 90% of the thrower's height. The magnitude of the velocity vector at launch is assumed to be 26 ms^{-1}.

4.3 Constraint

A constraint, g_1, is considered, as shown in Equation (19). This constraint means that the discus should make ground contact within the sector.

$$g_1 = \left| Y_{Line}\left(X_E\left(t_f\right)\right)\right| - \left| Y_E\left(t_f\right)\right| > 0 \qquad (19)$$

$$\left| Y_{Line}\left(X_E\left(t_f\right)\right)\right| = \tan\left(\frac{34.92°}{2}\right) \cdot X_E\left(t_f\right) \quad (20)$$

Here, $Y_{Line}(X_E(t_f))$ is the side line value of Y_E corresponding to $X_E(t_f)$, which is defined by Equation (20). The angle of 34.92° is shown in Figure 1.

4.4 Monte Carlo Method

In order to estimate $F2$ in Equation (18), the flight distance should be simulated around $FD_{candidate}$. The higher the value of n in Equation (18), the more convergent (constant) $F2$ will be, but the simulations will take a longer time to complete. It is possible to simulate FD_i with respect to a constant interval for each control and design variable. However, fourteen design variables are too many to do this. Therefore, the Monte Carlo method was applied. Monte Carlo methods rely on repeated random sampling to obtain numerical results. The simulation points are defined by the uniform random numbers in this study. The number of simulations (time for the simulation) can be controlled easily by changing n in Equation (18).
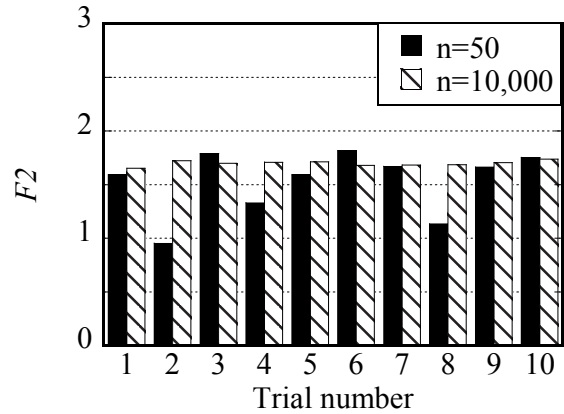

Figure 7: The n dependence of $F2$. In the case of n=50, the standard deviation among the ten trials is 0.29 meters. In the case of n=10,000, the standard deviation is 0.025 meters.

Figure 7 shows the dependence on n of $F2$. Ten trials (abscissa in Figure 7) were carried out, when the flight distance of the candidate for the optimal

solution, $FD_{candidate}$, was 78 meters. It can be seen that the value of $F2$ is almost constant among all of the trials in the case of n=10,000, while it is not constant in the case of n=50. In the case of n=50, the standard deviation among the ten trials is 0.29 meters. In this study, n=50 is applied to minimize the simulation time on the computer, although there is then an uncertainty of 0.29 meters (there is a possibility of an inaccuracy of 0.29 meters in $F2$ because of the smaller number of trajectory simulations n, which depends on the random number.).

The range for each design variable should be comparable with the human error in the competition and manufacturing error. Here, the ranges of the design variables are shown as 'Range for MC' in Table 1.

5 RESULTS AND DISCUSSIONS

The trade-off between $F1$ and $F2$ is shown in Figure 8. Although the lowest value (longest flight distance and smallest standard deviation) is ideal for each of the two objective functions, it is impossible for two objective functions to achieve their lowest values simultaneously. This is because the two objective functions conflict with each another. Therefore, multi-objective optimization involves a set of solutions, each of which is better regarding one objective function but worse regarding the others. These kinds of objective-conflicting solutions are called Pareto-optimal solutions, and represent the trade-off features among the objective functions. If $F1$ were a single objective (not optimized regarding $F2$), it would be possible to achieve a flight distance of 79.0 meters, which is 2 meters longer than the world record. However, it is not robust. There is a possibility of losing flight distance of 1.3 meters (=standard deviation), if the release condition slightly deviates from the optimal release condition. If $F2$ were a single objective (not optimized regarding $F1$), the flight would be robust for the deviation from the optimal release condition. However, the flight distance is merely 45.3 meters. The sweet spot, where both objective functions have better values simultaneously, is denoted by $\times$ in Figure 8. The flight distance is 78.8 meters at the sweet spot, while the standard deviation is 0.48 meters. Both the objective functions and the design variables are also shown in Table 2. The spin rate about the transverse axis is a relatively high R of 6.22 rev/s, the moment of inertia on the transverse axis is a relatively high I_T of 0.0058 kgm^2 and the

mass is almost the lowest permissible m_d of 1.007 kg.

The lift coefficients, C_L, as a function of AoA are shown in Figure 9. The open circles denote CFD results for the minimum case, in which all variables concerned with the sizes are the lowest. The open triangles denote CFD results in the maximum case, in which all variables are the highest. The closed triangles denote CFD results in the case of the sweet spot solution. It can be seen that the sweet spot solution is close to other cases, except around the stalling angle. Stalling for the sweet spot solution occurs at 34°, while stalling for other cases occurs at less than 29°.

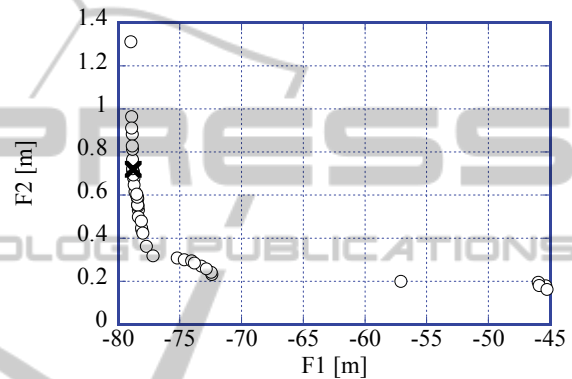

Figure 8: Trade-off (Pareto front) between both objective functions. An × denotes the sweet spot solution.

Table 2: Sweet spot solution.

Abb.	Sweet spot solution
$F1$	-78.82 m
$F2$	0.72 m
γ	37.70°
χ	11.07°
Ψ	1.78°
Θ	34.30°
Φ	36.29°
P	0.024 rev/s
Q	0.018 rev/s
R	6.22 rev/s
I_T	0.0058 kgm^2
m_D	1.007 kg
D_{FCA}	55.09 mm
R_{MR}	6.31 mm
THK	38.01 mm
w	181.51 mm

Figure 10 shows pressure distribution for three cases shown in Figure 9. The wind direction is from the left to the right. The wind speed was set at 30 ms^{-1}, and the angle of attack was set to 30°. The highest gauge pressure of 600 Pa is denoted by the red, while the lowest gauge pressure of -2000 Pa is

denoted by the blue. It can be seen that the pressure difference between the pressure side and the suction side becomes a maximum for the sweet spot solution (Figure 10-c). This means that the lift for the sweet spot solution becomes the highest of these three cases. The high pressure appears on the upstream side of the pressure side in all three cases. This is because the effective angle of attack on the upstream side becomes larger than that on the downstream side. The angle of incline for the sweet spot solution is 16.72°.
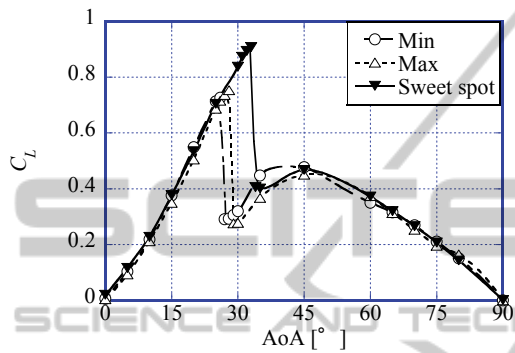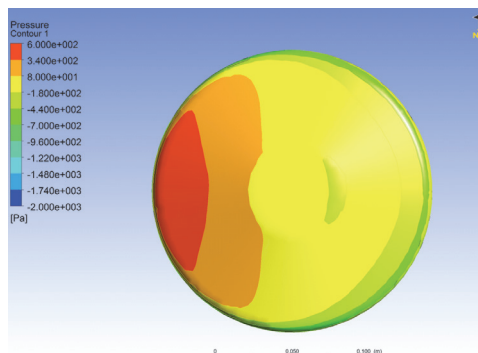

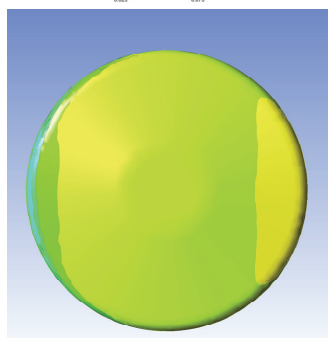Figure 9: *AoA* dependence of C_L.
Min: (D_{FCA}, R_{MR}, *THK*, *w*)= (*50, 5.85, 37, 180*)
Max: (D_{FCA}, R_{MR}, *THK*, *w*)= (*57, 6.45, 39, 182*)
Sweet spot: (D_{FCA}, R_{MR}, *THK*, *w*)= (*55, 6.3, 38, 181.5*)
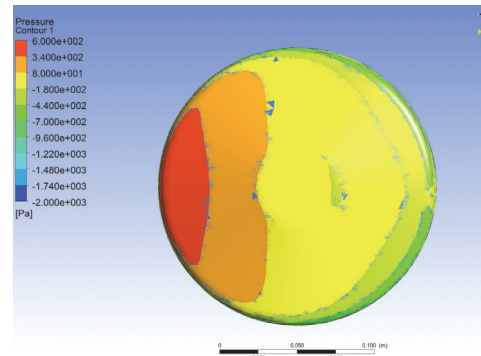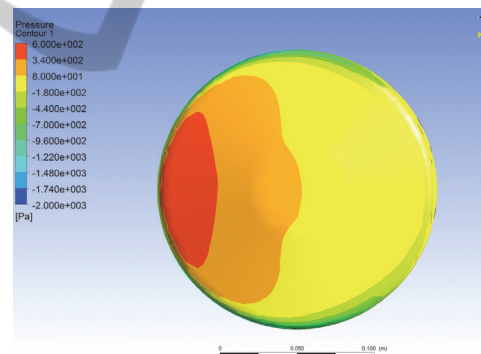
10-b) Minimum case. The upper is the pressure side, while the lower is the suction side.
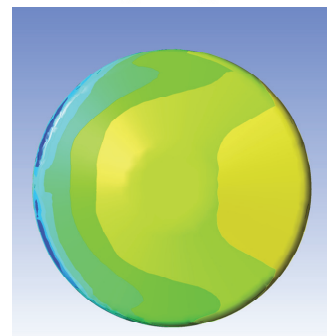(D_{FCA}, R_{MR}, *THK*, *w*)= (*50, 5.85, 37, 180*)

10-a) Maximum case. The upper is the pressure side, while the lower is the suction side.
(D_{FCA}, R_{MR}, *THK*, *w*)= (*57, 6.45, 39, 182*)

10-c) Sweet spot solution. The upper is the pressure side, while the lower is the suction side.
(D_{FCA}, R_{MR}, *THK*, *w*)= (*55, 6.3, 38, 181.5*)

Figure 10: Pressure distribution at AoA=30° and 30ms-1.

6 CONCLUSIONS

In this study, two objective functions are considered. One is the flight distance, the other is the robustness. The flight distance is the most important, but robustness is also important, especially for the world of competitive sports. Therefore, concurrent optimization of flight distance and robustness of discus throwing is carried out using a genetic algorithm. Fourteen design variables are considered, which include the skill of the thrower and the inherent features of the equipment. The design variables concerned with the skill and the equipment were treated concurrently. The conclusions are summarized as follows:

- There is a trade-off between flight distance and robustness.
- The longest flight distance that could be achieved was 79.0 meters. However, it is not robust. There is a possibility of losing flight distance of 1.3 meters, if the release condition slightly deviates from the optimal release condition.
- The flight distance is 78.8 meters at the sweet spot solution, where both objective functions of the flight distance and the robustness have better values simultaneously. There is a possibility of losing flight distance of 0.48 meters.
- The stalling angle for the sweet spot solution is relatively high. In other words, the maximum lift for the sweet spot solution becomes greater.
- At the sweet spot solution, the spin rate about the transverse axis is a relatively high R of 6.22 rev/s, the moment of inertia on the transverse axis is a relatively high I_T of 0.0058 kgm^2 and the mass is almost the lowest permissible m_d of 1.007 kg. The width is a relatively high w of 181.5mm, the thickness is 38mm, the metal rim radius is a relatively high R_{MR} of 6.3mm and the diameter of the flat center area is a relatively high D_{FCA} of 55mm.

ACKNOWLEDGEMENTS

REFERENCES

Deb, K., 2001. Multi-Objective Optimization using Evolutionary Algorithms. Wiley, New York

Hubbard, M. and Cheng, K., 2007. Optimal discus trajectories, J Biomechanics, 40, pp.3650-3659.

Leigh, S., Liu, H., Hubbard, M. and Yu, B., 2010. Individualized optimal release angles in discuss throwing, J Biomechanics, 43, pp.540-545.

Sasaki, D., and Obayashi, S., Efficient search for trade-offs by adaptive range multi-objective genetic algorithms, AIAA Journal of Aerospace Computing, Information, and Communication, 2005, pp.44-64.

Seo, K., Kobayashi, O., Murakami, M., Yorita, D., Nagai, H. and Asai, K., 2010. Simulation of the trajectory of a punted rugby ball taking into account the asymmetrical pressure distribution caused by the seams. *Journal of Visualization*, 13, pp. 97-105.

Seo K., Shimoyama K., Ohta K., Ohgi Y. and Kimura Y., 2012. Aerodynamic behaviour of a discus, *Procedia Engineering 34*, pp.92-97.

Stevens, B. and Lewis, F., 2003. *Aircraft control and simulation*, Wiley. Hoboken, New Jersey, 2nd edition.